The Astrophysical Journal, 871:198 (11pp), 2019 February 1 https://doi.org/10.3847/1538-4357/aaf862

High-mass Star Formation in the nearby Region G352.630-1.067. I. Parallax

Xi Chen[1,2], Jing-Jing Li[3], Bo Zhang[2], Simon P. Ellingsen[4], Ye Xu[3,5], Zhi-Yuan Ren[6], Zhi-Qiang Shen[2,5], and Andrej M. Sobolev[7]
[1] Center for Astrophysics, GuangZhou University, Guangzhou 510006, People's Republic of China; chenxi@gzhu.edu.cn
[2] Shanghai Astronomical Observatory, Chinese Academy of Sciences, Shanghai 200030, People's Republic of China; chenxi@shao.ac.cn
[3] Purple Mountain Observatory, Chinese Academy of Sciences, Nanjing 210008, People's Republic of China; jjli@pmo.ac.cn
[4] School of Natural Sciences, University of Tasmania, Hobart, TAS 7001, Australia
[5] Key Laboratory of Radio Astronomy, Chinese Academy of Sciences, Nanjing, JiangSu 210008, People's Republic of China
[6] National Astronomical Observatories, Chinese Academy of Science, Datun Rd. A20, Beijing, People's Republic of China
[7] Ural Federal University, 19 Mira street, 620002 Ekaterinburg, Russia
Received 2018 October 26; revised 2018 December 7; accepted 2018 December 11; published 2019 January 31

Abstract

Young or forming high-mass stars that are nearby and not within a cluster environment have the potential to provide fundamental insights into star formation. In this paper we report such a candidate (G352.630-1.067), for which we have measured the distance through very long baseline interferometry parallax observations of the associated 6.7 GHz class II methanol maser. We determine the distance to the source to be $0.69^{+0.10}_{-0.08}$ kpc, which makes it the second nearest high-mass star formation region (HMSFR) known, with only the Orion Nebula being closer. This may place this source, not within a Galactic spiral arm, but in the region between the Local and Sagittarius arms, indicating that molecular clouds in interarm regions may also generate high-mass stars. Kinematic association between this source and the Sagittarius Arm suggests that it may be located in a spur extending outward from this arm. Comparison with the known, nearby HMSFRs (distances less than 1 kpc), reveal that G352.630-1.067 is in a more isolated environment than others, hence providing an excellent candidate for investigations of the processes that form individual high-mass stars. We find a good spatial correlation between the 6.7 GHz methanol maser and high angular resolution images of the infrared outflow, suggesting that the class II methanol masers are closely associated with a jet/outflow in this source.

Key words: Galaxy: structure – masers – parallaxes – stars: formation

1. Introduction

The feedback processes from high-mass stars ($M > 8\,M_{\odot}$) have an important impact on their local environment, through outflows, stellar winds, and ionizing radiation. This impact extends over distances that are comparable to the typical dimensions of a star formation cluster (Kennicutt 2005). Despite high-mass stars playing an important role in galactic evolution, many of the details relating to their formation remain poorly understood. The largest impediment to improving our understanding of high-mass star formation is that the regions where they form are significantly more distant, compared to low-mass stars. The closest regions of isolated low-mass star formation are at distances of around 100 pc (e.g., Taurus 140 pc; Loinard et al. 2005), while the closest known high-mass star formation region is the Orion Nebula, more than four times further away (∼400 pc; see Menten et al. 2007 and Kounkel et al. 2017). On overall Galactic scales, the closest typical regions where high-mass stars form are at distances of around 2 kpc. A key and striking astronomical question is whether the Orion Nebula is truly the closest region where high-mass stars are currently forming, or whether there are closer regions. In addition, high-mass stars form almost exclusively in clusters, making it hard to distinguish between the properties of the cluster and those of individual members, even for nearby sources, such as the Orion Nebula.

The dynamical processes in high-mass star-forming regions are more complex than those in regions where only low-mass stars are forming. To explain how high-mass stars achieve their final masses, a number of scenarios have been proposed, such as monolithic collapse (analogous to isolated low-mass star formation; Yorke & Sonnhalter 2002; McKee & Tan 2003), and competitive accretion in a proto-cluster environment (Bonnell et al. 2001, 2004; Bonnell & Bate 2006). Both scenarios suggest that accretion is the primary mechanism through which high-mass stars form. Hence the role and physics of accretion are central to understand how high-mass stars form, yet in the cluster environment it remains poorly understood. This is mainly because we do not yet have the resolving power to trace the detailed accretion features directly for each of the scenarios, due to the large distances to high-mass star formation regions.

The factors described above demonstrate that searching for nearby and relatively simple (small cluster or isolated) high-mass star-forming regions is especially important in furthering our understanding of the critical processes in high-mass star formation. Within such regions it is possible to investigate in greater detail the physical and kinematic structures associated with a single high-mass young stellar object. In this paper, we identify a relatively simple high-mass star-forming region (G352.630-1.067) located at a distance of only 0.69 kpc. The distance has been determined using parallax measurements of the associated 6.7 GHz class II methanol maser with the Very Long Baseline Array (VLBA). This region provides an excellent candidate for investigating the detailed physical and kinematic processes during the formation of high-mass stars.

2. Massive Star-forming Region G352.630-1.067

Images from the *Spitzer* GLIMPSE II survey show that G352.630-1.067 is associated with extended emission in the

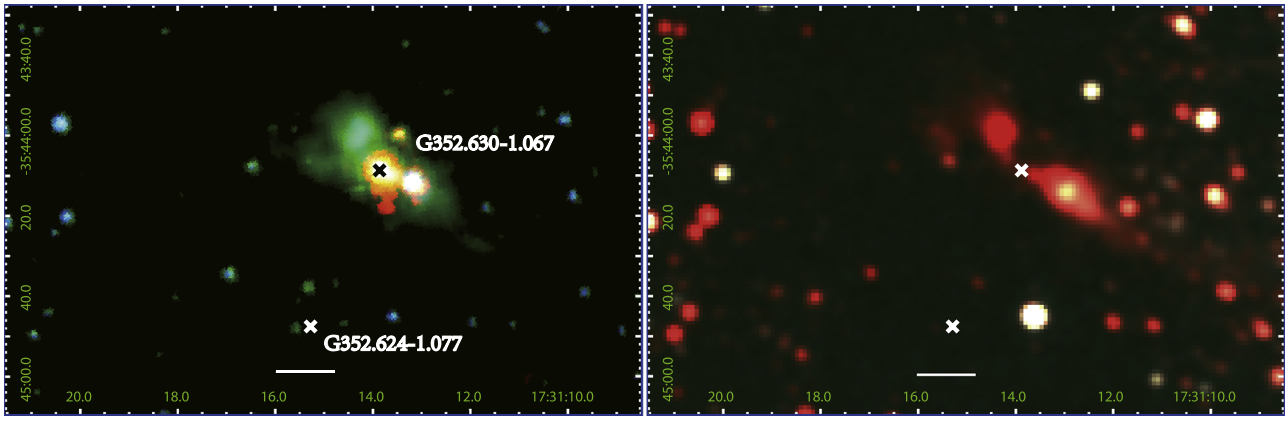

Figure 1. Three-color infrared images of G352.630-1.067. The left panel shows the three-color *Spitzer* IRAC image composite with 8.0 μm in red, 4.5 μm in green, and 3.6 μm in blue. The right panel shows the three-color 2MASS image composite with *Ks*-, *H*-, and *J*-bands in red, green, and blue, respectively. The position of the 6.7 GHz class II methanol maser (known to subarcsecond accuracy) is marked by "×" in the two panels. The spatial linear scale of 0.2 pc (at a distance of 0.69 kpc; see the text) is given by the horizon line in the bottom of each panel.

4.5 μm band (Chen et al. 2013a). The strong and extended emission at 4.5 μm is thought to be produced by shock-excited H_2 and CO molecules when protostellar outflows interact with the ambient ISM (Cyganowski et al. 2008). These regions are commonly referred to as extended-green objects (EGOs) due to the 4.5 μm band often being assigned to the green channel in three-color images made using *Spitzer* IRAC data. The 2MASS near-infrared image also shows corresponding extended emission in the 2 μm *Ks*-band which is attributed to emission from shock-excited H_2. Figure 1 shows *Spitzer* IRAC and 2MASS *JHK* three-color composite images for G352.630-1.067. From this figure, it can be seen that this source shows very extended emission in the 4.5 and 2 μm bands with a total angular extent greater than 1′ along the northeast to southwest direction. The central bright object at 8 μm has an associated 6.7 GHz class II methanol maser and as these are known to be exclusively tracers of the early stages of high-mass star formation (Xu et al. 2008; Breen et al. 2013), this indicates that it is a high-mass young stellar object (YSO). Furthermore, the location of the infrared point source at the center of the extended 4.5 and 2 μm emission suggests that it is likely the driving source of the outflow. 95.1 GHz class I methanol maser emission has also been detected toward G352.630-1.067 (Chen et al. 2013a). The population inversion for class I methanol masers is due to collisions (e.g., Leurini et al. 2016). They are typically observed in regions where there are weak shocks in cool molecular gas, such as due to the expansion of H II regions, or at the interface between outflows and molecular gas (e.g., Voronkov et al. 2014). The detection of a class I methanol maser is consistent with the presence of a molecular outflow in G352.630-1.067 because this source is a young high-mass YSO (see below) and is not associated with a H II region. Previous investigations have shown that more than 50% of EGOs are associated with class II and/or class I methanol masers (e.g., Cyganowski et al. 2009; Chen et al. 2011, 2013a). This supports the general consensus that EGOs correspond to MYSOs at a very early evolutionary stage, with ongoing outflow activity.

Thermal molecular line emission from a number of species have been detected in this source (Chen et al. 2013b). Single dish observations of a number of dense gas tracers (including HNC, CS, ^{13}CS, and C^{34}S) show that the systemic velocity $V_{\rm LSR}$ of G352.630-1.067 is -0.2 ± 2.0 km s^{-1}. This velocity is

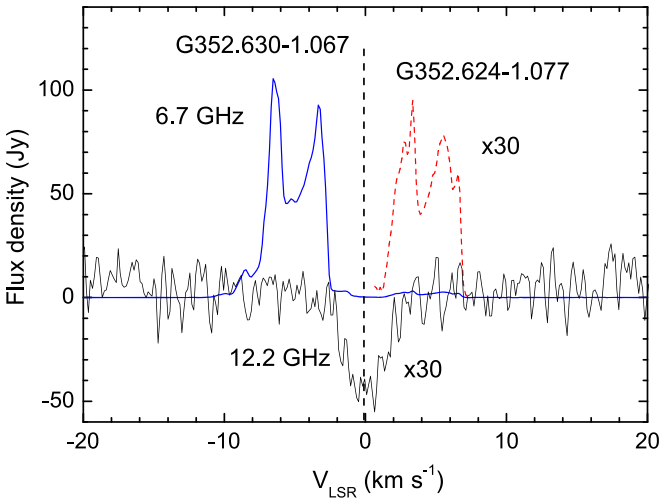

Figure 2. Spectra of the 6.7 and 12.2 GHz methanol transitions toward G352.630-1.067 detected by Shanghai Tianma 65 m radio telescope. The dashed line denotes the systemic velocity. To clearly show weaker spectral components we have scaled flux density by a factor of 30 times for the whole 12.2 GHz spectrum and for the redshifted part of the 6.7 GHz emission (associated with G352.624-1.077).

the mean of the peak velocities of the molecular lines and the quoted uncertainty is the typical FWHM. With this systemic $V_{\rm LSR}$, the near kinematic distance of this source is estimated to be ∼750 pc, using the new flat Galactic rotation model of Reid et al. (2014). The high galactic latitude of this source (for a 6.7 GHz methanol maser; Green et al. 2017) and the extended infrared outflow structures also suggest that this source is likely to be relatively close, because the typical angular size of EGO sources in *Spitzer* images is only about 10″. However, the estimated kinematic distance of this source may not be very accurate, due to its proximity to galactic longitude $l = 0°$, where the line-of-sight velocity of all sources is predicted to be small in a circular rotation model. This paper reports an accurate distance measurement to this source obtained from annual parallax measurements of the 6.7 GHz class II methanol maser toward this source.

Figure 2 presents the methanol spectra of both the 6.7 and 12.2 GHz class II transitions recently detected with the Shanghai Tianma 65 m radio telescope (X. Chen et al. 2018, in preparation). The rms noises ($1\sigma_{\rm rms}$) of the Tianma

Table 1
Details of the Epochs Observed

Code	Source	Epoch 1	Epoch 2	Epoch 3	Epoch 4	Epoch 5	Epoch 6
BC219	G352.63−01.07	15 Mar 21	15 Aug 22	15 Dec 06	16 Mar 28	18 Mar 15	18 Apr 21

Table 2
Positions and Brightnesses

Source	R.A. (J2000) (^{h} ^{m} ^{s})	Decl. (J2000) (° ′ ″)	ϕ (°)	Brightness (Jy beam^{-1})	V_{LSR} (km s^{-1})	NW beam (mas, mas, deg)
G352.630−1.067	17 31 13.8875	−35 44 08.714	⋯	51.9	−3.4	4.7 × 4.3 @ −39
J1736−3400	17 36 57.8248	−34 00 30.442	2.1	0.035	⋯	5.3 × 4.3 @ 16
J1733−3722	17 33 15.1932	−37 22 32.390	1.7	0.549	⋯	5.3 × 4.3 @ 16

Note. ϕ is the angular separation between the maser and the calibrator. The maser absolute position, the peak brightness, the size and P.A. of the naturally weighted (NW) beam are listed for the first epoch for each source. The P.A. of the beam is defined as east of north.

observations are 0.05 Jy and 0.025 Jy (at a spectral resolution of 0.15 km s^{-1}) for the 6.7 GHz and 12.2 GHz methanol transitions, respectively. The 6.7 GHz methanol maser emission shows a double-peak profile, with emission at velocities less than −2 km s^{-1} much stronger than that at positive velocities. The methanol multibeam (MMB) survey observations toward this region (Caswell et al. 2010) detect two regions of 6.7 GHz methanol maser emission with an offset of 42″ between them. The maser emission at velocities less than −2 km s^{-1} is from G352.630-1.067 and is associated with the bright IR source at the center of Figure 1, while the emission at positive velocities is from the offset source G352.624-1.077, located near the southern edge of Figure 1. There is no 6.7 GHz methanol maser emission at the systemic velocity of the source, but there is absorption in the 12.2 GHz methanol transition, which shows a maximum at the systemic velocity. From the single dish Tianma observations we cannot determine the distribution, or the location of the strongest absorption for the 12.2 GHz methanol transition. Hence we are unable to determine whether it is associated with the 6.7 GHz class II and/or the 95 GHz class I methanol masers. However, the presence of absorption shows the presence of a radio continuum source (or sources) behind the foreground methanol molecular gas. Since the 6.7 GHz masers are all blueshifted with respect to the systemic velocity, this suggests that the maser is located in gas which is outflowing toward the observer. Breen et al. (2012) searched for 12.2 GHz methanol maser emission toward this source and also did not detect any emission in their observations in 2008 June and December with 5σ upper limits of 0.75 and 0.80 Jy respectively. Breen et al. (2010) proposed a maser-based evolutionary timeline, which suggested that the 6.7 GHz methanol maser luminosity increases with age and that the 12.2 GHz methanol masers are associated with older, more evolved 6.7 GHz maser sites. The absence of 12.2 GHz methanol maser emission associated with G352.630-1.067 suggests that it is a relatively young high-mass YSO.

3. Parallax Observations toward G352.630-1.067

To accurately determine the distance to G352.630-1.067, we can utilize the astrometric measurement of the trigonometric parallax through the technique of very long baseline interferometry (VLBI) phase referencing. This technique has been successfully applied to measure trigonometric parallaxes of Galactic 22 GHz water and 12.2 GHz methanol maser sources in the Bar and Spiral Structure Legacy (BeSSeL) Survey using the VLBA (see Reid et al. 2009). In addition to the 22 GHz water masers and 12.2 GHz methanol masers, the 6.7 GHz methanol masers have been successfully used in parallax measurements of massive star-forming regions (e.g., Rygl et al. 2010; Krishnan et al. 2015, 2017; Xu et al. 2016). Adopting a similar technique, we have used the VLBA (program BC219) to conduct six epochs of phase-referencing observations of the 6.7 GHz methanol masers in G352.630-1.067 over the period from 2015 March to 2018 April. For each epoch the observations consisted of a single 4.5 hr block. The observations were undertaken near the peaks of the sinusoidal trigonometric parallax curve in the east–west direction. The specific observing dates are given in Table 1. The phase center for the maser source was α = 17:31:13.91, β = −35:44:08.7 (J2000), which was obtained from the MMB project (Caswell et al. 2010).

Using the phase-referencing technique, the observations were performed with a switching time of 55 s alternating between the maser target (typically achieving 30 s of on-source data) and two nearby (∼2°) compact radio quasars J1736-3400 and J1733-3722, which were used as background sources. Table 2 lists the positions of the maser target and background sources. One major difficulty with the observations was that the sources are at a very southerly decl. for the VLBA and because of this it was only possible to observe the target source for about 3 hr each session, as that is the duration for which it is accessible by 5–7 VLBA antennas at elevations of >15°. For each epoch the average on-source time for the maser target was about 1.5 hr.

The data were recorded with four adjacent bands of 16 MHz bandwidth, in each dual circular polarization with 2-bit sampling. The data were correlated with the VLBA correlator in Socorro, NM, using two passes: (1) all observed sources were correlated in continuum mode with 32 channels for each 16 MHz band; (2) only the frequency band containing a maser signal (a single 16 MHz bandwidth) was correlated with 2048 spectral channels, resulting in a channel separation of 7.8 kHz or 0.41 km s^{-1} at 6.7 GHz. The data were reduced using the Astronomical Image Processing System, following the standard data reduction pathway for astrometric, phase-referencing mode observations of masers described in Reid et al. (2009). As the maser emission is stronger than the two background quasars, we used the maser source as the phase reference

Table 3
Detailed Results of Parallax and Proper Motion

Background Source	V_{LSR} (km s^{-1})	Detected Epochs	Parallax (mas)	μ_x (mas yr^{-1})	μ_y (mas yr^{-1})
			G352.630−1.067		
J1736−3400	−3.4	111111	1.315 ± 0.169	−1.15 ± 0.10	−1.97 ± 0.26
	−4.1	111111	1.251 ± 0.229	−0.53 ± 0.14	−1.26 ± 0.19
	−5.5	111111	1.434 ± 0.120	−0.22 ± 0.07	−0.83 ± 0.24
	Combined fit		1.331 ± 0.101		
	Average			−0.53 ± 0.05	−1.31 ± 0.13
J1733−3722	−3.4	101111	1.547 ± 0.371	−1.42 ± 0.12	−1.37 ± 0.45
	−4.1	101111	1.476 ± 0.323	−0.81 ± 0.11	−0.68 ± 0.41
	−5.5	101111	1.760 ± 0.494	−0.49 ± 0.17	−0.25 ± 0.46
	Combined fit		1.594 ± 0.224		
	Average			−0.98 ± 0.07	−0.77 ± 0.25
	Combined fit		1.444 ± 0.105		
	Average			−0.68 ± 0.05	−1.20 ± 0.13

calibrator during the phase-referencing procedure. The maser spot at $V_{LSR} = -3.4$ km s^{-1} was selected as the phase reference because it was considerably stronger and was detected on all baselines across all epochs. Images of the background calibrator were formed using only data from the IF containing maser. This is because when data from other IFs were included in the background calibrator images the parallax fitting error increased. (see Section 4.1). The positions of the maser source and background calibrators extracted from the image data are listed in Table 2.

We performed geodetic-like observations using ∼15 ICRF quasars whose positions are known to better than 1 mas. These quasars were observed with a bandwidth synthesis frequency setup, for a duration of 30 minutes. These data were taken in left circular polarization with four 16 MHz bands that spanned 480 MHz, a frequency range from 4.412 to 4.892 GHz and from 6.876 to 7.356 GHz within *C* band. These bands were configured with frequencies offset by 0, 80, 320, and 480 MHz. One of these blocks was placed at the beginning and end of each of the six epochs. This allows us to estimate the residual tropospheric zenith delay with an uncertainty <1 cm (Reid et al. 2009). In addition, another important contribution to the residual delay is from the ionosphere. Although we can remove the estimated ionospheric delay determined from global models based on GPS total electron content observations (Walker & Chatterjee 1999); unfortunately, there still remains a residual ionospheric zenith delay at the level of a few centimeters at 6.7 GHz. This residual ionospheric delay limits parallax accuracy to ∼0.1 mas (see Reid et al. 2017) and we give a detailed discussion as to how this uncertainty affects our parallax results in Section 5.1.

4. Results

4.1. Parallax Measurements

The parallaxes and proper motions were determined from the changes in position of the maser spots relative to the background sources. The parallax sinusoid in both R.A. and decl. coordinates, were fitted for the parallax and a linear proper motion in each coordinate. The formal position errors determined from the images do not include systematic errors, which typically dominate over thermal noise. The systematic errors are mainly due to the residual ionospheric zenith delay, but in some cases are due to maser variation and source structure. This results in high reduced χ^2 values for the fits. Therefore error floors were added in quadrature to the position uncertainties in the fits. Different error floors were used for R.A. and decl. data and were adjusted until reduced χ^2 values close to unity were obtained for both coordinates.

During the fitting, we first carried out parallax and proper motion fits for each of the maser spots detected at more than five epochs relative to each of the two background sources. Although we detected six maser spots persisting over at least five epochs, only three maser spots, those at V_{LSR} of −3.4, −4.1, and −5.5 km s^{-1} can be used for phase referencing in the final fitting. This is mainly because some maser spots are weak and possibly blended in position and frequency. In addition, we found that the positions determined for the background source J1733-3722 for the second epoch are significantly offset from the parallax sinusoid that is clearly present in the other data. If we add the second epoch data of J1733-3722 to the fits, the parallax using the phase reference channel data (V_{LSR} of −3.4 km s^{-1}) from J1733-3722 is 0.302 ± 0.497 mas (i.e., the uncertainty significantly exceeds the amplitude of the parallax). This result is quite different from that which we obtain when we exclude the second epoch data for J1733-3722 (1.547 ± 0.371 mas; see Table 1). We have not been able to determine the reason for the discrepant position of J1733-3722 in the second epoch, but speculate that it may be because the observations for this calibrator were at a very low elevation, causing larger than normal errors due to residual uncertainty in the atmospheric delay calibration. However, as it is clearly aberrant, exclusion of the second epoch data for J1733-3722 from the fitting seems reasonable. Therefore, in the overall fits we have discarded the data for this calibrator source in the second epoch.

The fitting results for each maser spot relative to each of the two background sources are summarized in Table 3. The right-hand panel in Figure 3 shows that the fit results for each of the single maser spots and epochs are in very good agreement. A second series of fits were produced independently for each of the two background sources, which assumes the same parallax, but allows different proper motions for the three maser spots. The results of these fits are also given in Table 3 and they are consistent with each other within the error bars. Finally, we produced a fit that combines all the data from the three maser

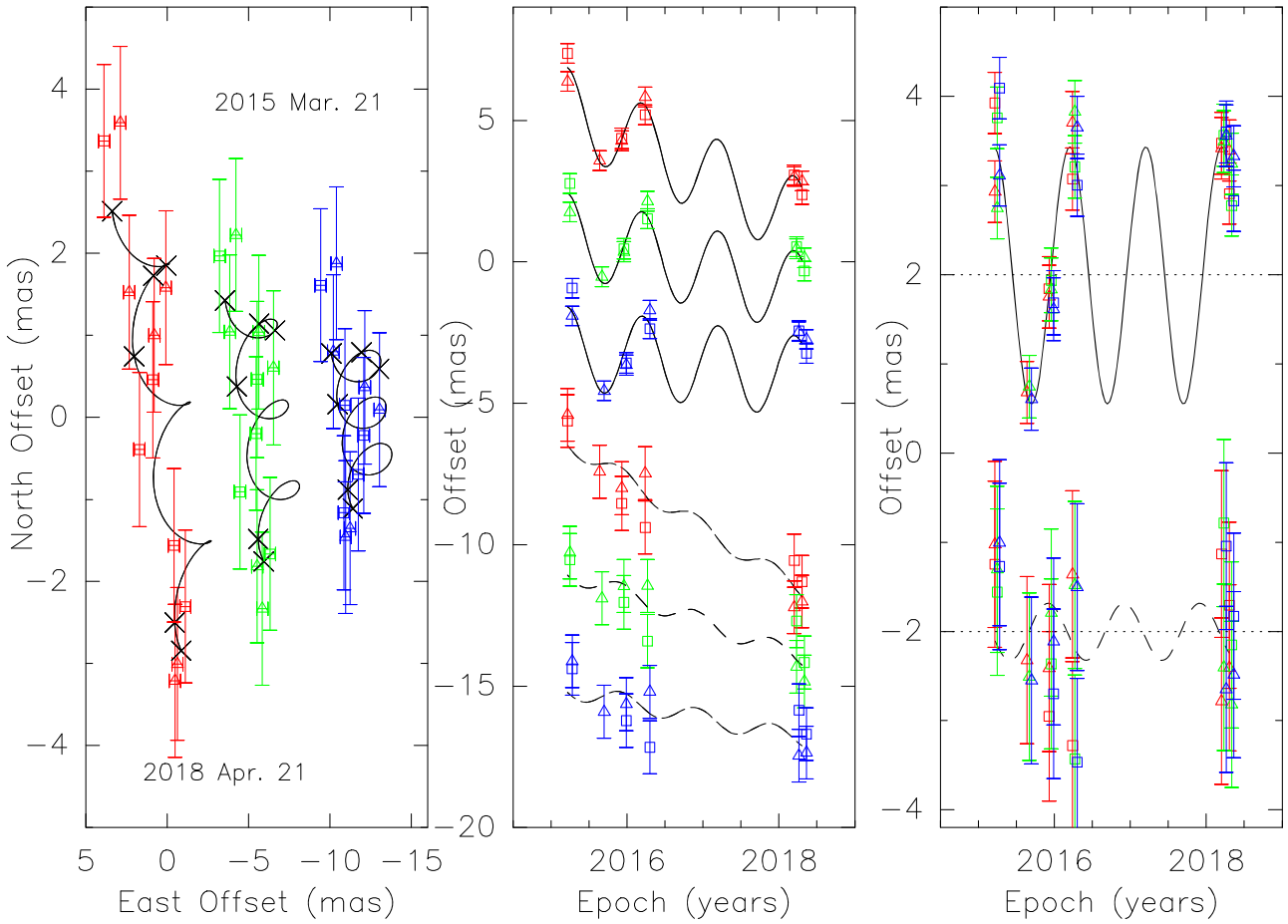

Figure 3. Parallax and proper motion data and fits for G352.630−1.067. Plotted are data for the three maser spots at $V_{\rm LSR} = -3.4$ km s^{-1} (red), −4.1 km s^{-1} (green), and −5.5 km s^{-1} (blue) relative to the two background sources J1736−3400 (triangle) and J1733−3722 (square), respectively. Left panel: positions on the sky with the first and last epochs labeled. Notably, the different position coverage in the north among the three maser spots reflects their different proper motions. The expected positions from the parallax and proper motion fit are indicated (crosses). Middle panel: east (solid line) and north (dashed line) position offsets and best parallax and proper motions fits vs. time. Right panel: same as the middle panel but with the best-fit proper motions removed to more clearly illustrate the parallax sinusoid.

Table 4
Parallaxes and Proper Motions of G352.63−01.07

Source	ϕ (mas)	D (kpc)	μ_x (mas yr^{-1})	μ_y (mas yr^{-1})	$V_{\rm LSR}$ (km s^{-1})
352.630−1.067	1.444 ± 0.182	$0.69^{+0.10}_{-0.08}$	−0.68 ± 0.05	−1.20 ± 0.13	−0.2 ± 2

spots for the two background sources. The results of the parallax and proper motion fits are displayed in Figure 3, and the final results are listed in Table 4.

The parallax of G352.630-1.067 from the final fit utilizing all the data simultaneously is measured to be 1.44 ± 0.18 mas, corresponding to a distance of $0.69^{+0.10}_{-0.08}$ kpc. The adopted uncertainty for the parallax is the error of the combined fit multiplied by $\sqrt{N}$, where $N = 3$ is the number of maser spots used in the fit. This astrometric distance is consistent with the near kinematic distance of this source (∼750 pc) using the new flat Galactic rotation model of Reid et al. (2014).

From the fitting results, we found that the proper motions of the three maser spots are quite different. The difference between the maser spots with $V_{\rm LSR}$ of −3.4 and −5.5 km s^{-1} is about −1 mas yr^{-1} for both the east–west and north–south directions. This difference reflects the internal motions of the maser spots relative to the systemic motion of the system. We use the mean of the proper motions of the three maser spots $(\bar{\mu}_x, \bar{\mu}_y) = (-0.68 \pm 0.05, -1.20 \pm 0.13)$ mas yr^{-1} as an estimate of the absolute proper motion of the exciting star, corresponding to −2.2 ± 0.2 km s^{-1} and −3.9 ± 0.4 km s^{-1} at a distance of 0.69 kpc, respectively.

We also made an attempt to analyze the methanol data at positive velocities associated with G352.624-1.077. We achieved a detection of a methanol spot with $V_{\rm LSR}$ of 6.7 km s^{-1} at the position of $\alpha = 17{:}31{:}15.3166$, $\beta = -35{:}44{:}47.597$ (J2000) from our observations. But we cannot determine the distance to this maser source because, with no maser components stronger than 1 Jy, its emission is too weak for parallax measurements with the current data.

4.2. Relative Proper Motions of Methanol Maser Features

Usually, the high angular and velocity resolution of VLBI observations, partly resolves individual masing clouds. A maser "feature" is constructed by combining the spatially overlapping emission observed across contiguous spectral

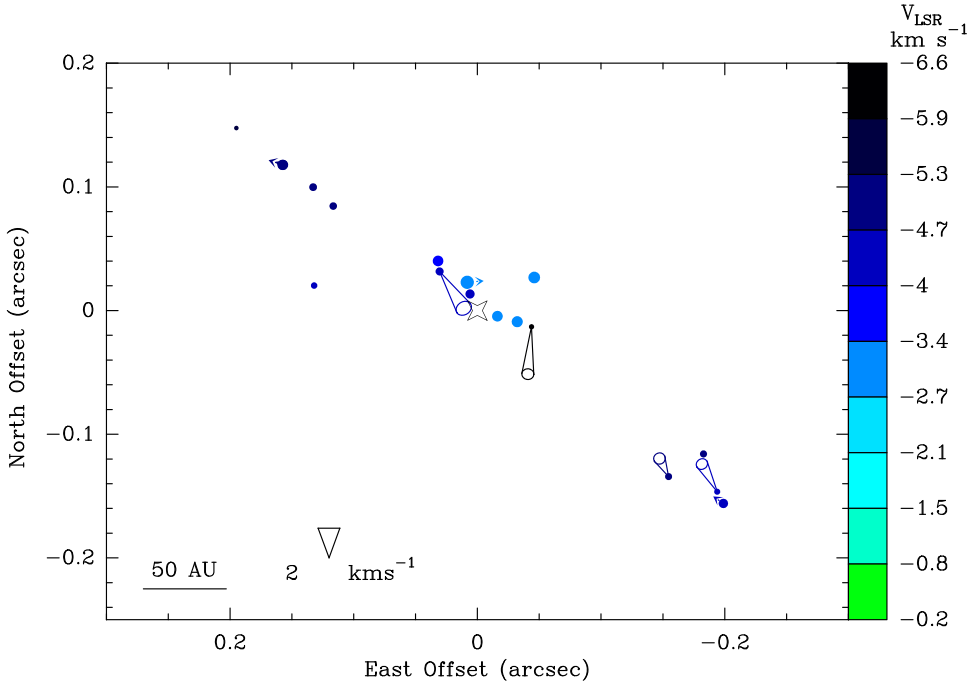

Figure 4. Spatial distribution and proper motions of 6.7 GHz methanol maser features relative to the center of motion. Different color tones are used to indicate the maser LSR velocities, according to the color scale on the right-hand side of the plot. The symbol sizes are scaled logarithmically with feature intensity. The cones indicate the 3D velocities of the methanol maser features. Points without an associated cone have been detected over only one or two epochs and the associated proper motion cannot be computed or is considered unreliable. The cone opening angle gives the 1σ uncertainty on the proper motion direction. The length of the cone is proportional to the velocity, with the amplitude scale indicated in the lower left corner of the figure.

Table 5
Parameters of VLBA 6.7 GHz Methanol Maser Features in G352.63−01.07

Feature Number	Epochs of Detection	$V_{\rm LSR}$ (km s^{-1})	S_v (Jy)	$\Delta\alpha$ (mas)	$\Delta\delta$ (mas)	V_α (km s^{-1})	V_δ (km s^{-1})
0	111111	...	...	−8.90 ± 0.10	−25.53 ± 0.20	...	...
1[a]	111111	−3.07	75.6	−0.69 ± 0.11	−2.67 ± 0.20	−1.11 ± 0.17	0.10 ± 0.93
2[a]	111111	−5.25	7.9	148.24 ± 0.11	92.27 ± 0.20	0.98 ± 0.27	0.32 ± 0.75
3[a]	111111	−4.05	4.2	−207.80 ± 0.12	−181.46 ± 0.21	0.68 ± 0.27	0.47 ± 0.71
4	101001	−4.35	0.8	−202.83 ± 0.13	−171.98 ± 0.22	1.03 ± 0.25	1.86 ± 0.24
5	111111	−4.07	2.1	21.64 ± 0.12	6.12 ± 0.21	−1.63 ± 0.29	−2.49 ± 0.70
6	111111	−5.23	7.7	148.66 ± 0.11	92.29 ± 0.20	0.48 ± 0.36	0.22 ± 0.57
7	111101	−6.56	0.6	−52.67 ± 0.11	−38.61 ± 0.21	0.25 ± 0.17	−3.19 ± 1.20
8	111111	−5.13	1.2	−163.51 ± 0.13	−159.75 ± 0.23	0.61 ± 0.08	1.21 ± 0.32
9	100000	−5.49	0.4	185.97 ± 0.16	122.05 ± 0.25	0.00 ± 0.00	0.00 ± 0.00
10	010000	−3.48	10.2	20.23 ± 0.13	12.33 ± 0.23	0.00 ± 0.00	0.00 ± 0.00
11	010100	−3.12	10.2	−29.45 ± 0.16	−32.84 ± 0.27	0.00 ± 0.00	0.00 ± 0.00
12	000100	−3.06	13.5	−41.34 ± 0.16	−36.08 ± 0.26	0.00 ± 0.00	0.00 ± 0.00
13	000100	−5.25	1.8	123.68 ± 0.15	72.69 ± 0.26	0.00 ± 0.00	0.00 ± 0.00
14	000100	−5.25	1.6	107.43 ± 0.17	57.41 ± 0.26	0.00 ± 0.00	0.00 ± 0.00
15	000010	−3.02	21.2	−56.59 ± 0.16	−2.19 ± 0.27	0.00 ± 0.00	0.00 ± 0.00
16	000011	−4.78	1.3	−173.53 ± 0.12	−105.36 ± 0.23	0.00 ± 0.00	0.00 ± 0.00
17	000011	−4.42	0.9	141.34 ± 0.13	30.70 ± 0.24	0.00 ± 0.00	0.00 ± 0.00
18	000010	−4.28	3.8	−4.68 ± 0.12	−15.52 ± 0.22	0.00 ± 0.00	0.00 ± 0.00

Note.
[a] The maser feature contains the maser spots used in the fitting for the parallax and proper motions.

channels. A maser feature can reflect the kinematics of a maser cloud more accurately. We have used the methods described in Li et al. (2012) and Sanna et al. (2010a, 2010b) to identify individual maser features, derive their parameters (e.g., position and flux density), and measure their relative proper motions. In total, 18 maser features are identified across the six epochs of observation. Information on these maser features (including velocities, positions, and flux densities) are listed in Table 5 and denoted with numbers 1–18. The spatial distributions of the maser features is presented in Figure 4. Their positions are obtained from the first epoch of their appearance. All these detected maser features come from G352.630-1.067 and are blueshifted with regard to the systemic velocity (-0.2 km s^{-1}) of the source.

There are eight maser features that are detected in more than three epochs (denoted with numbers 1–8 in Table 5). We have analyzed the proper motions for these eight maser features, adopting the methods in Li et al. (2012) and Xu et al. (2013), we calculate the proper motions relative to the common motion center of these features. The common center of these features is listed in Table 5 as feature number 0 and shown in Figure 4. The typical velocity of these features is less than 3 km s^{-1}. Almost all maser features for which we have proper motion estimates show velocity vectors that are aligned approximately along the direction of elongation of the maser distribution. The relative proper motions are in opposite directions for the masers near the center of the distribution compared to those in the lower right corner of Figure 4. This reflects the difference in the interior motions between the two groups of maser features.

5. Discussions

5.1. Uncertainties in Parallax Measurements

The approach used in the fitting of the parallax gives an estimate of the distance with an accuracy of 0.18 mas (12.5% of the distance) for G352.630-1.067 (see Section 4.1). This astrometric uncertainty is consistent with the expected value without corrections for the residual dispersive ionospheric delays at the 6.7 GHz, as described in Section 3. Reid et al. (2017) suggested that the uncompensated ionospheric delays result in systematic errors in the measured relative-position shifts between maser and quasar, affecting the parallax and proper motion estimates. Based on their observing data, they found that separate parallax measurements for a maser based on different quasars typically showed a "parallax gradient" on the sky. They developed analysis methods to deal with the problem of position gradients across different background sources. Significant improvements in parallax accuracy (to a level of 0.03 mas) for 6.7 GHz methanol maser data were achieved with the new methods (see Reid et al. 2017). Such accuracy is far better than that obtained in our analysis.

To investigate whether our measurement accuracy could be improved through implementation of the Reid et al. (2017) techniques, we used their methods to reanalyze our data. Because there were only two background sources observed, Method-2 described in Reid et al. (2017) was used for the analysis, as this approach only requires two quasars to work. However, we cannot obtain a reasonable fit for the parallax and proper motions with this approach. Our analysis shows a larger error (more than 50%) for the parallax when we try to use Method-2 from Reid et al. (2017) with our data, so we have not used it in further analysis. One possible reason for being unable to obtain an adequate fit through this approach is that the VLBA antennas were working at low elevations (15°–20°) during the observations, and the Reid et al. (2017) techniques may not work well for sources at lower elevations. Honma et al. (2008) have noticed that the dependence of astrometric accuracy with elevation shows a $\sec Z \times \tan Z$ dependence because of the greater effect of the residual atmospheric delay errors, where Z is the source zenith angle.

5.2. Galactic Location

Based on the parallax measurements, the source G352.630-1.067 is located between the Local and Sagittarius spiral arms. Figure 5 shows the location of this source in the Milky Way. However, it should be noted that the only data point samples the minimum in the R.A. parallax sinusoid (see Figure 3). This may result in a larger uncertainty in the parallax measurement. For a 3σ deviation in the parallax measurement (1.44 ± 0.18 mas; see Table 4), the parallax would be $\sim$0.9 mas (1.1 kpc distance). At this distance it would not be unreasonable to associated the source with the Sagittarius spiral arm. Assuming a lifetime of less than 10^5 yr for sources associated with 6.7 GHz methanol masers (see Breen et al. 2010), the source G352.630-1.067 can have only moved a few parsecs from its natal cloud, as it has a peculiar motion of $<$20 km s^{-1} (the calculations of peculiar motions are discussed below). Therefore, this source must still be close to its birthplace, which is well away from the two nearby spiral arms. This also suggests that some high-mass stars form in molecular clouds in the regions between the major arms.

The phenomenon of high-mass stars forming in regions between the major spiral arms has been reported in previous work. For example, Xu et al. (2018a, 2018b) found that there are a number of O-type stars identified from the *Gaia* DR2 data set that are located between the Local and Sagittarius arms. The locations of five high-mass star-forming regions associated with 6.7 GHz methanol or 22 GHz water masers in a spur, emanating from the Sagittarius Arm near $l \approx 50°$ and bridging toward the Local Arm, has been inferred from parallax measurements of their masers (see Xu et al. 2016). This further confirms that there is significant high-mass star formation activity in molecular clouds in the regions between nearby arms.

5.3. Peculiar Motions

The combination of the parallax and proper motion measurements (see Section 4.1), along with the systemic line-of-sight velocity, can be used to determine the three-dimensional (3D) peculiar motions relative to circular motion around the Galactic center. The systemic $V_{\rm LSR}$ of G352.630-1.067 is about -0.2 ± 2.0 km s^{-1}, estimated from the mean of the peak velocities traced by many thermal dense gas tracers (see Section 2). The method for calculating the systemic $V_{\rm LSR}$ here is different from that adopted in previous analyses that considered velocities (or kinematic modeled velocities) of the masers (e.g., Xu et al. 2013; Zhang et al. 2013; Wu et al. 2014). However, this estimate is reasonable, because unlike H_2O and CH_3OH masers, which have additional motions with respect to the central stars, thermal dense gas tracers are physically and kinematically tied to the central star. For G352.630-1.067 the 6.7 GHz methanol maser components are detected only at blueshifted velocities, thus they do not provide a reliable estimate of the systemic velocity of the source.

The peculiar motion components (U_s, V_s, W_s) of a given source can be obtained by subtracting the effects of Galactic rotation at the location of the source from the measured space motions. The three motion components U_s, V_s, W_s are defined to be the motion toward the Galactic center, in the direction of Galactic rotation, and toward the north Galactic pole, respectively. To estimate the circular rotation components at a given location in the Galaxy, we assume a flat Galactic rotation curve, with Galactic constants $R_0 = 8.31 \pm 0.16$ kpc, $\Theta_0 = 241 \pm 8$ km s^{-1} and solar motion values of, $U_\odot = 10.5 \pm 1.7$ km s^{-1}, $V_\odot = 14.4 \pm 6.8$ km s^{-1}, and $W_\odot = 8.9 \pm 0.9$ km s^{-1} (the "Univ" model in Reid et al. 2014). The estimated peculiar motions for G352.630-1.067 determined using this approach are listed in Table 6.

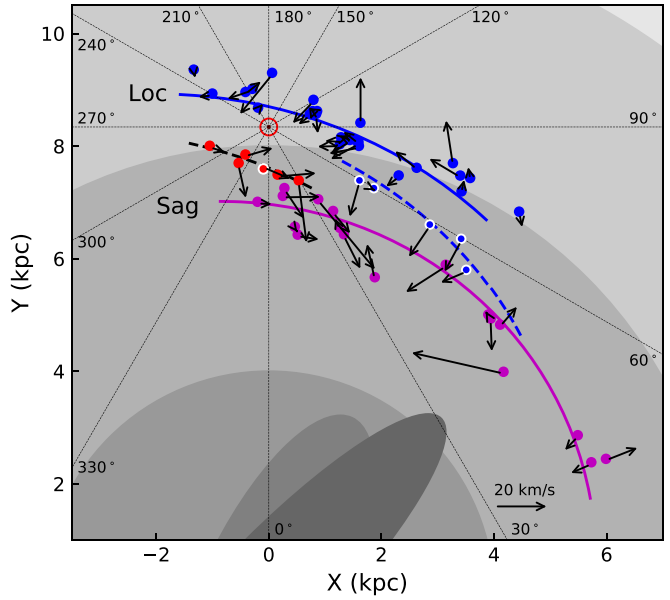

Figure 5. Locations and peculiar motions of HMSFRs determined by trigonometric parallax. The target G352.630−1.067 in this paper is indicated by a red circle with a white outline. Maser sources associated with the Perseus (blue circles) and Sagittarius (magenta circles) arms, and those in the spur between the two arms (blue circles with white outlines) detected by Xu et al. (2016) are also presented. The red circles show the five O-stars detected by *Gaia* in the space between the Perseus and Sagittarius arms with longitudes close to the Galactic center. The peculiar motion vectors have been obtained by transforming to a reference frame rotating with the Galaxy, using values of $R_0 = 8.31$ kpc and $\Theta_0 = 241$ km s^{-1} (Reid et al. 2014). A motion scale of 20 km s^{-1} is indicated in the bottom left corner. The galaxy is viewed from the north galactic pole and rotates clockwise. The Sun is marked with an open red circle and reference Galactic Longitude directions are indicated. The background is extracted from Figure 2 of Xu et al. (2016).

Table 6
Peculiar Motion

Source	U_s (km s^{-1})	V_s (km s^{-1})	W_s (km s^{-1})
G352.630−1.067	4.6 ± 3.0	10.6 ± 0.9	8.8 ± 0.3

Note. These motions are relative to the Galactic "Univ" model and the Solar motion from Reid et al. (2014), as described in the text.

The peculiar motion measurements indicate that the G352.630-1.067 region is moving toward the Galactic center and rotating more quickly (by 10.7 km s^{-1}) than for circular Galactic orbits at this radius. The peculiar motions for more than 100 sources in the Galactic arms have been determined from parallax measurements (e.g., Xu et al. 2013; Zhang et al. 2013; Choi et al. 2014; Sato et al. 2014; Wu et al. 2014). To investigate possible kinematic associations with arms, we compare the peculiar motion of G352.630-1.067 with those of sources in the two nearby arms (Local and Sagittarius). Note that the peculiar motion component, V_s is critically related to the adopted $V_\odot$ value. For comparison, we have recalculated the peculiar motions of sources in the two arms using the same Galactic constants and solar motion values as those used in this paper for the G352.630-1.067 peculiar motion. We find that the averages of motion in the direction of Galactic rotation $\bar{V}_s$ are -3.1 ± 0.7 km s^{-1} and 6.2 ± 1.4 km s^{-1} for Local arm sources (Xu et al. 2013) and Sagittarius arm sources (Wu et al. 2014), respectively. The peculiar motions of these sources are shown in Figure 5. Comparing these motions, we find that G352.630-1.067 has a similar motion in the direction of Galactic rotation to the sources in the Sagittarius arm. For sources in the longitude range close to the Galactic center all of the Sagittarius Arm sources show positive V_s values. In contrast, the peculiar motion of G352.630-1.067 is in the opposite direction to that of the sources in the Local Arm. This suggests that G352.630-1.067 may have a kinematic association with the Sagittarius Arm and hence that it is located in a spur extending outward from the Sagittarius Arm into the interarm space.

Spurs are often observed in external galaxies (Elmegreen 1980; Scoville et al. 2001; La Vigne et al. 2006) and are believed to have comparable lifetimes to spiral arms. In the Milky Way, a significant spur structure branching between the local and Sagittarius spiral arms has been identified from a combination of parallax measurements of masers (see Xu et al. 2016). This spur has a length of >2 kpc, and emanates from the Sagittarius Arm at around Galactic Longitude $50° < l < 70°$. The pitch angle of this spur is 18°.3 (see Figure 2 in Xu et al. 2016). Our current work suggests that, another spur may be present, traced by the regions extending from the Sagittarius Arm (based on the kinematic association between the source G352.630-1.067 and the Sagittarius Arm), close to the direction of Galactic center. We cannot at present determine any details of this spur (such as pitch angle or length) due to the association of only one high-mass star formation region (HMSFR) found to date. The U_s motion component of G352.630-1.067 (∼5 km s^{-1}) shows that it is moving toward the Sagittarius Arm. This is very similar to those sources in the spur in the region from $50° < l < 70°$ (see Figure 5), all of which show motion toward the Sagittarius Arm. This similarity seems to support our potential newly identified spur extended from the Sagittarius Arm near the direction of the Galactic center. The *Gaia* DR2 data set shows five O-type stars in the longitude range $-40° < l < 30°$ that are close to the G352.630-1.067 region and have proper motion measurements (represented by red circles in Figure 5). The peculiar motions of these O-stars have a similar direction to the G352.630-1.067 maser region, so both the O-stars and the specific HMSFR we are studying here may be linked with a spur structure (see Figure 5). However, much more observational evidence of HMSFRs or OB-type stars in this region are required to determine if this is the case.

5.4. Comparison with Other Nearby HMSFRs

Besides the Orion cloud, there are four well-known HMSFRs that have been determined to be at distances of less than 1 kpc (G108.18+05.51/L1206; G109.87+02.11/Cep A; L1287 and G213.70-12.60/Mon R2). Parallax measurements place all of these sources in the Local Arm (Rygl et al. 2010; Xu et al. 2016). All of these regions have associated 6.7 GHz methanol masers and to investigate the differences between our target and those sources, we have compared the infrared images from the *WISE* and 2MASS surveys. Figure 6 shows the infrared images of the four well-known HMSFRs, which can be compared with the infrared images of G352.630-1.067 (Figure 1). It is clear that these other four sources represent more complicated cluster environments.

Figure 6 shows that each of these four HMSFRs exhibits outflows traced by extended emission in the *WISE* 4.6 μm band and the 2MASS K_s band. However, unlike G352.630-1.067,

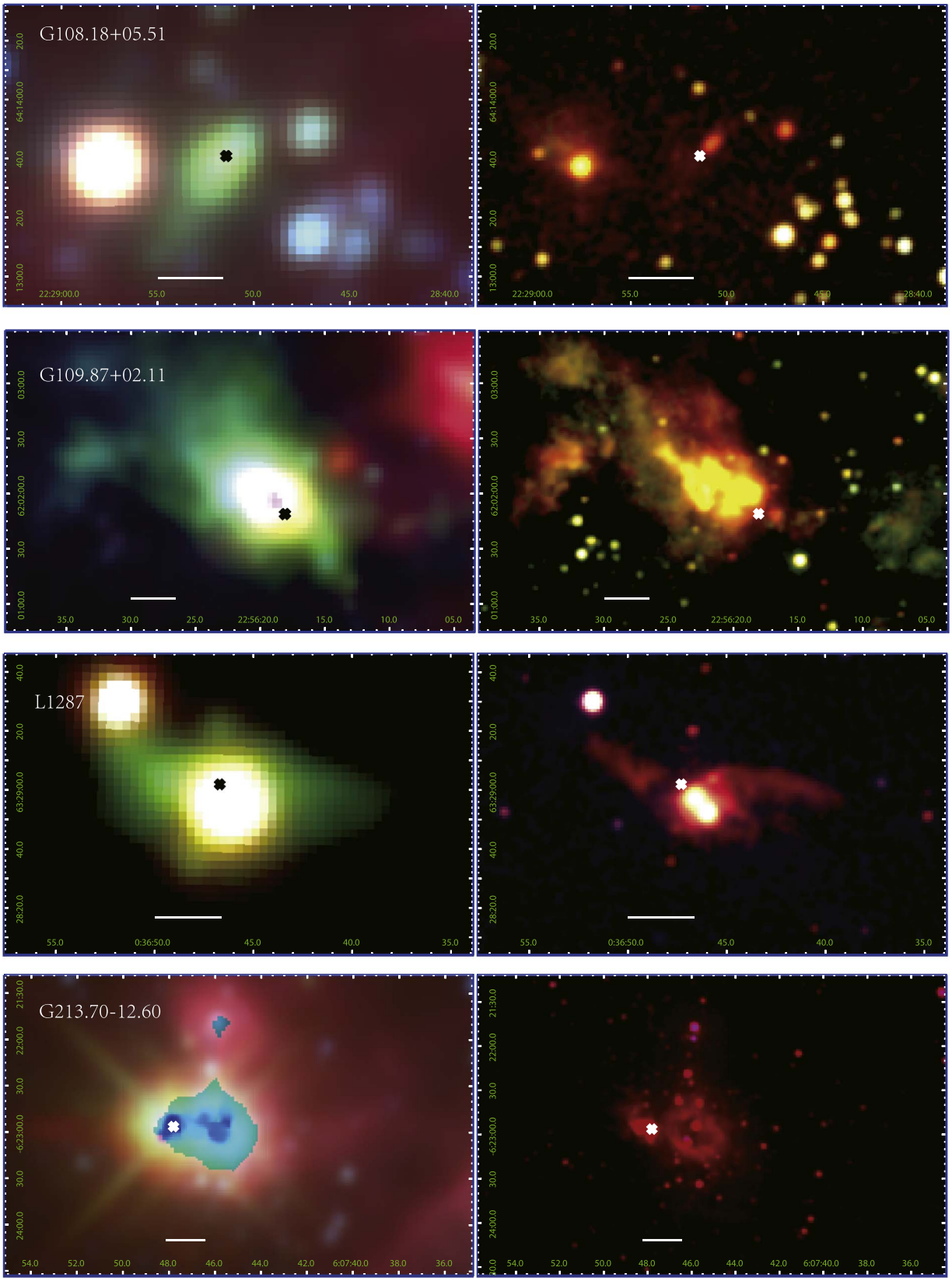

Figure 6. Three-color composite infrared images of four known HMSFRs at distances of less than 1 kpc. For each source, the left-hand panel shows the three-color *WISE* image composite with 12.0 μm in red, 4.6 μm in green, and 3.4 μm in blue; the right-hand panel shows the three-color 2MASS image composite with *Ks*-, *H*-, and *J*-bands in red, green, and blue, respectively. The position of the 6.7 GHz class II methanol maser (known to subarcsecond accuracy) is marked by "×" in the two infrared images of each source. A spatial linear scale of 0.1 pc is indicated by the horizon line in the bottom of each panel. The typical cluster size for the four HMSFRs is 0.3–0.5 pc.

their infrared outflows are not collimated (except for G108.18 +05.51 which shows a collimated outflow along the southeast to northwest direction traced by the extended *WISE* 4.6 μm emission). This may be because complicated cluster environments reduce the degree of collimation outflows compared to high-mass stars (such as G352.630-1.067), which form in molecular clouds in interarm regions.

The above comparison with known HMSFRs located at distances (less than 1 kpc), shows that G352.630-1.067 is an excellent candidate for further studies of the physical and kinematic structures around an individual high-mass YSO at moderate spatial resolution ($\sim$1″). Such observations will be very helpful in investigating high-mass star formation with little or no impact due to intra-cluster interactions. We have performed millimeter interferometric observations of dust continuum and molecular lines toward this source with the Submillimeter Array and will report the results of these observations in a subsequent paper (Paper II).

5.5. Methanol Masers Associated with Jets

Class II methanol masers are known to trace the region close to the high-mass protostar. However, the specific location and association with kinematic structures are still the topic of debate. Some class II methanol masers have been shown to exhibit line, arc, or ring-like distributions and it has been suggested that the methanol masers are associated with either jet/outflow-driven shocks (e.g., Walsh et al. 1998) or a rotating disk or torus (e.g., Norris et al. 1998; Phillips et al. 1998; Bartkiewicz et al. 2009). Measurements of the internal proper motions of methanol masers support an association with rotating disk structures in some sources (e.g., Sanna et al. 2010a, 2010b; Moscadelli et al. 2011; Sugiyama et al. 2014), and outflow motion in other sources (e.g., Rygl et al. 2010; Sugiyama et al. 2011). For G352.630-1.067, the methanol maser emission is distributed along a linear structure oriented from southwest to northeast (see Figure 4). The large-scale infrared outflows, revealed in the *Spitzer* and 2MASS images (see Figure 1), show the same position angle as the methanol maser distribution. So G352.630-1.067 appears to be an example of a class II methanol maser that is closely associated with a jet/outflow from the exciting star.

Figure 4 shows that the relative proper motions of the maser features nearly align with the direction of the maser distribution. This alignment suggests that the maser features move in a material flow along the structure, rather than as part of a rotating disk or torus structure. Some maser features show contrary motion directions; however, this is likely because the proper motions have been determined with respect to the motion center, rather than the driving star. Further observational evidence for the association of the methanol maser with a jet or outflow in G352.630-1.067 is that the maser features are all blueshifted and hence located on the nearside of the source with a component of motion directed along the line of sight.

6. Summary

Measuring the trigonometric parallax of the 6.7 GHz methanol masers in the G352.630-1.067 region with VLBI phase referencing, we find it to be at a distance of $0.69^{+0.10}_{-0.08}$ kpc. This makes it one of the closest high-mass star formation regions and shows that it may not be within a known Galactic spiral arm, but in the region between the Local and Sagittarius arms. This measurement, combined with data for a number of O-stars detected by *Gaia* toward the region around this source, demonstrates that high-mass star formation activity can happen in interarm regions. This source is in a more isolated environment than other nearby HMSFRs, possibly due to the simple molecular cloud environment in interarm regions. Overall, this source is nearby and not within a complicated cluster environment, hence providing a candidate for investigating the physical and dynamical details of individual high-mass star formation.

We thank the anonymous referee for helpful comments that improved the manuscript. This work was supported by the National Natural Science Foundation of China (11590781, 11873002, 11590780), Australian Research Council Discovery project number DP180101061 funded by the Australian Government, and the major scientific research project of Guangdong regular institutions of higher learning (2017KZDXM062).

ORCID iDs

Simon P. Ellingsen https://orcid.org/0000-0002-1363-5457

References

Bartkiewicz, A., Szymczak, M., van Langevelde, H. J., et al. 2009, A&A, 502, 155
Bonnell, I. A., & Bate, M. R. 2006, MNRAS, 370, 488
Bonnell, I. A., Bate, M. R., Clarke, C. J., & Pringle, J. E. 2001, MNRAS, 323, 785
Bonnell, I. A., Vine, S. G., & Bate, M. R. 2004, MNRAS, 349, 735
Breen, S. L., Ellingsen, S. P., Caswell, J. L., et al. 2012, MNRAS, 421, 1703
Breen, S. L., Ellingsen, S. P., Caswell, J. L., & Lewis, B. E. 2010, MNRAS, 401, 2219
Breen, S. L., Ellingsen, S. P., Contreras, Y., et al. 2013, MNRAS, 435, 524
Caswell, J. L., Fuller, G. A., Green, J. A., et al. 2010, MNRAS, 404, 1029
Chen, X., Ellingsen, S. P., Shen, Z. Q., Titmarsh, A., & Gan, C. G. 2011, ApJS, 196, 9
Chen, X., Gan, C.-G., Ellingsen, S. P., et al. 2013a, ApJS, 206, 9
Chen, X., Gan, C.-G., Ellingsen, S. P., et al. 2013b, ApJS, 206, 22
Choi, Y. K., Hachisuka, K., Reid, M. J., et al. 2014, ApJ, 790, 99
Cyganowski, C. J., Brogan, C. L., Hunter, T. R., & Churchwell, E. 2009, ApJ, 702, 1615
Cyganowski, C. J., Whitney, B. A., Holden, E., et al. 2008, AJ, 136, 2391
Elmegreen, D. M. 1980, ApJ, 242, 528
Green, J. A., Breen, S. L., Fuller, G. A., et al. 2017, MNRAS, 469, 1383
Honma, M., Tamura, Y., & Reid, M. J. 2008, PASJ, 60, 951
Kennicutt, R. C. 2005, in IAU Symp. 227, Massive Star Birth: A Crossroads of Astrophysics, ed. R. Cesaroni et al. (Cambridge: Cambridge Univ. Press), 3
Kounkel, M., Hartmann, L., Loinard, L., et al. 2017, ApJ, 834, 142
Krishnan, V., Ellingsen, S. P., Reid, M. J., et al. 2015, ApJ, 805, 129
Krishnan, V., Ellingsen, S. P., Reid, M. J., et al. 2017, MNRAS, 465, 1095
La Vigne, M. A., Vogel, S. N., & Ostriker, E. C. 2006, ApJ, 650, 818
Leurini, S., Menten, K. M., & Walmsley, C. M. 2016, A&A, 592, A31
Li, J. J., Moscadelli, L., Cesaroni, R., et al. 2012, ApJ, 749, 47
Loinard, L., Mioduszewski, A. J., Rodrguez, L. F., et al. 2005, ApJL, 619, 179
McKee, C., & Tan, J. 2003, ApJ, 585, 850
Menten, K. M., Reid, M. J., Forbrich, J., & Brunthaler, A. 2007, A&A, 474, 515
Moscadelli, L., Cesaroni, R., Rioja, M. J., Dodson, R., & Reid, M. J. 2011, A&A, 526, 66
Norris, R. P., Byleveld, S. E., Diamond, P., et al. 1998, ApJ, 508, 275
Phillips, C. J., Norris, R. P., Ellingsen, S. P., & McCulloch, P. M. 1998, MNRAS, 300, 1131
Reid, M. J., Brunthaler, A., Menten, K. M., et al. 2017, AJ, 154, 63
Reid, M. J., Menten, K. M., Brunthaler, A., et al. 2009, ApJ, 693, 397
Reid, M. J., Menten, K. M., Brunthaler, A., et al. 2014, ApJ, 783, 130
Rygl, K. L. J., Brunthaler, A., Reid, M. J., et al. 2010, A&A, 511, 2
Sanna, A., Moscadelli, L., Cesaroni, R., et al. 2010a, A&A, 517, 71
Sanna, A., Moscadelli, L., Cesaroni, R., et al. 2010b, A&A, 517, 78
Sato, M., Wu, Y. W., & Immer, K. 2014, ApJ, 793, 72
Scoville, N. Z., Polletta, M., Ewald, S., et al. 2001, AJ, 122, 3017

Sugiyama, K., Fujisawa, K., Doi, A., et al. 2011, PASJ, 63, 53
Sugiyama, K., Fujisawa, K., Doi, A., et al. 2014, A&A, 562, 82
Voronkov, M. A., Caswell, J. L., Ellingsen, S. P., Green, J. A., & Breen, S. L. 2014, MNRAS, 439, 2584
Walker, C., & Chatterjee, S. 1999, VLBA Scientific Memo 23, https://library.nrao.edu/vlbas.shtml
Walsh, A. J., Burton, M. G., Hyland, A. R., & Robinson, G. 1998, MNRAS, 301, 640
Wu, Y. W., Sato, M., Reid, M. J., et al. 2014, A&A, 566, 17
Xu, Y., Bian, S. B., Reid, M. J., et al. 2018a, A&A, 616, L15
Xu, Y., Hou, L.-G., & Wu, Y.-W. 2018b, RAA, 18, 146
Xu, Y., Li, J. J., Hachisuka, K., et al. 2008, A&A, 485, 729
Xu, Y., Li, J. J., Reid, M. J., et al. 2013, ApJ, 769, 15
Xu, Y., Reid, M., Dame, T., et al. 2016, SciA, 2, e1600878
Yorke, H., & Sonnhalter, C. 2002, ApJ, 569, 846
Zhang, B., Reid, M. J., & Menten, K. M. 2013, ApJ, 775, 79